Modeling and optimal design for static shape control of smart reflector using simulated annealing algorithm

Zhi Wang, Yuyan Cao, Yongzhi Zhao and Zhichen Wang

Abstract

This article presents a finite element formulation for static shape control and optimal design of smart reflector with distributed piezoelectric actuators. The finite element model is developed based on the higher-order shear deformation theory where the displacement field in the model accounts for a parabolic distribution of the shear strain, and the shear correction factor is not involved. The Hamilton variational principle is used to formulate the governing equation of the system. A four-node element with seven mechanical degrees of freedom for each node and one electrical potential degree of freedom for each piezoelectric actuator element is used in the finite element formulation. The optimization model for finding the optimal control voltages is derived, and the control voltages can be determined using Lagrange multipliers. The optimal design of actuator locations using simulated annealing algorithm is also investigated. Finally, numerical examples are given to demonstrate the effectiveness of the present model and optimization scheme. The obtained results show that the use of piezoelectric actuators for static shape control of smart reflector can greatly improve the root mean square error, and the optimal location of actuators can be determined effectively using simulated annealing algorithm.

Keywords

Actuator, optimization, smart reflector, static shape control, simulated annealing

Introduction

As large-aperture reflectors are able to collect more photons for observations at higher spatial and/or spectral resolutions, high performance and lightweight reflectors are required by advanced systems, such as large ground-based astronomical telescopes and antennas (Chen et al., 2000).

With the development of lightweight reflector, the large-aperture composite reflectors made of carbon fiber-reinforced plastic (CFRP) are able to be applied to optical telescope (Chen and Romeo, 2004). The reflector will become more "floppy" due to its large aperture; thus, the active correction of surface deformation caused by gravity, temperature gradient, or fabrication errors is inevitable.

The review articles by Kapuria et al. (2010) and Khandan et al. (2012) give the details of the theories proposed for modeling laminated composite structures. In general, two different theories have been used to model composite structures: the single-layer theory and discrete-layer theory. In the single-layer approach, the layers in the composites are supposed to be one equivalent single layer, whereas in the discrete-layer theory, each layer is considered in the analysis.

Chee et al. (2000) developed a composite finite element formulation based on the higher-order shear displacement field coupled with a layerwise linear electric potential using the Hamilton variational energy principle. The obtained results showed that the eight-node element was found superior to the four-node element for a thin structure.

Lage et al. (2004) proposed a finite element model based on layerwise theories for piezo-laminated plate structures. The Reissner mixed variational principle is used to formulate the model.

Balamurugan and Narayanan (2007) have presented a higher-order shear flexible piezo-laminated C1 QUAD-8 multilayer smart composite finite element. There are 48 mechanical degrees of freedom and 9

Changchun Institute of Optics, Fine Mechanics and Physics, Chinese Academy of Sciences, Changchun, China

Corresponding author:
Yuyan Cao, Changchun Institute of Optics, Fine Mechanics and Physics, Chinese Academy of Sciences, Dong Nanhu Road 3888, Changchun 130033, China.
Email: yuyan_cao@126.com

electric potential degrees of freedom per piezoelectric layer in the element, and the electric potential is assumed to vary quadratic over the thickness.

Elshafei and Alraiess (2013) presented a finite element model based on the simple higher-order shear deformation theory to analyze composite beams with distributed piezoelectric actuators. The electric potential is modeled as a function of the thickness and the length of the beam element.

Several researchers have studied the shape control of smart structures. Frecker (2003) reviewed the studies in development of design methodologies and application of formal optimization methods to the design of smart structures and actuators. Gupta et al. (2010) reviewed the various optimization criteria used by researchers for optimal placement of sensors and actuators on the smart structures.

Paradies and Hertwig (1999) have studied the shape control of adaptive composite reflectors using moment actuator concept. The moment actuator can provide continuous actuation spatially distributed across the surface which is different from the conventional piston actuator used in adaptive or active optics. Chee et al. (2002) studied the static shape control of composite plates and developed a perturbation build-up voltage distribution algorithm to determine the optimal voltage of piezoelectric actuators. Sun and Tong (2005) studied the design optimization of actuator patterns for static shape control of composite plates with piezoelectric actuator patches and employed energy optimization–based method for finding the optimal control voltages.

Moita et al. (2006, 2008) presented a finite element formulation based on the third-order shear deformation theory for active control of laminate structures. The genetic algorithm and simulated annealing (SA) algorithm were used to optimize the lamination sequence and the location of piezoelectric actuators.

Hwan-Sik and Washington (2005, 2010) and Hwan-Sik (2013) have investigated mechanically reconfigurable reflector antennas, and the deformable reflector can change the radiation pattern for the optimal usage of the radiation power. In their research, a mathematical formulation for the shape optimization problem is developed, and the deformation of the structure is expressed in terms of actuation values of a set of actuators using finite element modeling. The analytical solution for the optimal actuation values is obtained in a closed form. A simple longitudinally actuated one-dimensional bar and a mechanically deformable reflector antenna structure are chosen as the validity examples.

Wang and Li (2014) have investigated the active vibration control of cable net structures, and the H2-norm strategy is presented for the optimization of sensor or actuator locations in controlled flexible cable net structures.

Wang et al. (2014) have discussed the static shape control of smart reflector, in which the Kirchhoff classical laminated theory is adopted to model the structure, and the Lagrange multipliers method is used to determine the solution to the optimization model for shape control. The work is the preliminary research of the present work, which mainly focuses on the effectiveness of the Lagrange multipliers method in solving the optimization problem of static shape control for smart reflector considering actuator voltage limitation.

In the present work, static shape control and optimal design of smart reflector structure with piezoelectric actuators are investigated. First, the finite element model based on the higher-order shear deformation theory is developed. The Hamilton variational principle is used to formulate the governing equation of the system. Second, the constrained optimization model for finding the optimal control voltages is established, and Lagrange multipliers are employed to deal with the voltage limitation. The optimal design of actuator locations using SA algorithm is also investigated. Finally, illustrative examples are presented to demonstrate the capabilities and efficiency of the developed model and optimization algorithm in static shape control of smart reflector.

Finite element formulation of smart reflector

The structure of smart reflector considered in this study (see Figures 1 and 2) consists of lightweight sandwich composite reflector substrate and piezoelectric actuator patches. The lightweight composite reflector is made up of two thin CFRP facesheets (i.e. the top and bottom facesheets) and a moderate thick hexagon aluminum honeycomb core. The cross section of the overall structure is shown in Figure 3. The total thickness is $t_f + t_a$ (with actuator patches) or t (without actuator patches), where t_f is the thickness of top or bottom facesheet and t_a is the thickness of piezoelectric actuator. The top and bottom facesheets have the same material properties and geometry, composed by 1–Nth and $(N + 2)$th–$(2N + 1)$th layers, respectively. The $(N + 1)$th and $(2N + 2)$th layers are honeycomb and actuator layers, respectively.

These piezoelectric actuator patches attached to the bottom facesheet of smart reflector constitute a new type of moment actuator (see Figure 4(a)). In some applications, moment actuators provide a competitive alternate approach to the conventional piston type of actuators (see Figure 4(b); Mehta, 1990).

These so-called moment actuators have many advantages as follows (Liu, 1993):

1. It seems to provide effective global transverse deflections, whereas piston actuator tends to provide large deflections locally;
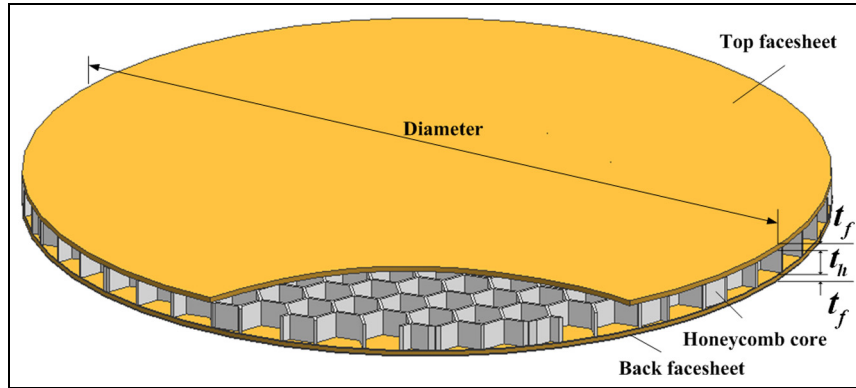2. It may be attached directly onto the back sheet of a lightweight mirror without the stand-off

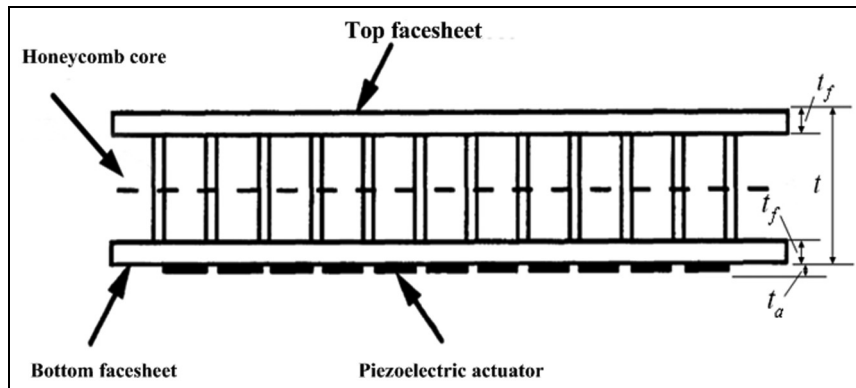**Figure 1.** Structure of smart reflector.

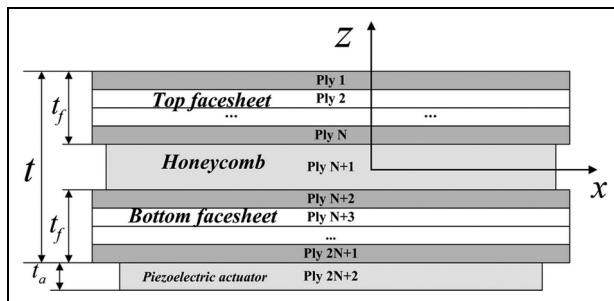**Figure 2.** Smart mirror with moment actuator.

Figure 3. Cross section of smart reflector.

devices. However, the piston actuator must be supported by the stand-off devices, which increases the weight of the reflector system.

In order to simplify the mathematical description for the behavior of smart mirror structure system, we make the assumptions that the actuator patches are perfectly bonded on the bottom facesheet, and the top and bottom facesheets are perfectly bonded on both sides of the honeycomb core, respectively.
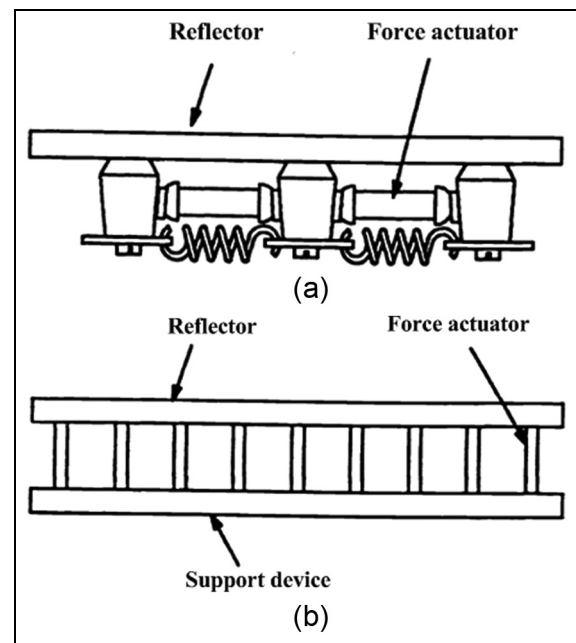

Figure 4. Two different actuation approaches for smart reflector: (a) with moment actuators and (b) with piston actuators.

Displacement and strain field

The assumed displacement field for the smart reflector is that of the higher-order shear deformation theory developed by Reddy (1999) (see Figure 5). The advantages of the higher-order shear deformation theory are as follows: (1) it is suitable for both thick and thin composite structures; (2) it does not need shear correction factors; and (3) transverse shear effects can be modeled, and it captures a parabolic transverse shear across the thickness of the structure.

The displacement field based on the higher-order theory can be expressed by

$$u(x, y, z) = u_0(x, y) + z\varphi_x(x, y) - c_1 z^3 \left(\varphi_x + \frac{\partial w_0}{\partial x} \right)$$

$$v(x, y, z) = v_0(x, y) + z\varphi_y(x, y) - c_1 z^3 \left(\varphi_y + \frac{\partial w_0}{\partial x} \right)$$

$$w(x, y, z) = w_0(x, y) \tag{1}$$

where (u_0, v_0, w_0) and (φ_x, φ_y) are the displacement components and the rotations of transverse normal on the plane $z = 0$, respectively. The $\partial w_0 / \partial x$ and $\partial w_0 / \partial y$ are the slopes of the tangents of the deformed middle surface in the x and y directions, and $c_1 = 4/3h^2$, where h is the total thickness of the laminate.

The strain components associated with the displacements in equation (1) are represented by

$$\varepsilon_{xx} = \frac{\partial u(x, y, z)}{\partial x} = \frac{\partial u_0}{\partial x} + z\frac{\partial \varphi_x}{\partial x} - c_1 z^3 \left(\frac{\partial \varphi_x}{\partial x} + \frac{\partial^2 w_0}{\partial x^2} \right)$$

$$\varepsilon_{yy} = \frac{\partial v(x, y, z)}{\partial y} = \frac{\partial v_0}{\partial y} + z\frac{\partial \varphi_y}{\partial y} - c_1 z^3 \left(\frac{\partial \varphi_y}{\partial y} + \frac{\partial^2 w_0}{\partial y^2} \right)$$

$$\gamma_{xy} = \frac{\partial v}{\partial x} + \frac{\partial u}{\partial y} = \frac{\partial u_0}{\partial y} + \frac{\partial v_0}{\partial x} + z \left(\frac{\partial \varphi_x}{\partial y} + \frac{\partial \varphi_y}{\partial x} \right)$$
$$- c_1 z^3 \left(\frac{\partial \varphi_x}{\partial y} + \frac{\partial \varphi_y}{\partial x} + 2\frac{\partial^2 w_0}{\partial x \partial y} \right) \tag{2}$$

$$\gamma_{yz} = \frac{\partial w}{\partial y} + \frac{\partial v}{\partial z} = \varphi_y + \frac{\partial w_0}{\partial y} - 3c_1 z^2 \left(\varphi_y + \frac{\partial w_0}{\partial y} \right)$$

$$\gamma_{xz} = \frac{\partial w}{\partial x} + \frac{\partial u}{\partial x} = \varphi_x + \frac{\partial w_0}{\partial x} - 3c_1 z^2 \left(\varphi_x + \frac{\partial w_0}{\partial x} \right) \tag{3}$$

Constitutive equations

The linear constitutive relations for each orthotropic laminate layer of the smart reflector in the global coordinates can be written as

$$\begin{bmatrix} \sigma_{xx} \\ \sigma_{yy} \\ \tau_{yz} \\ \tau_{xz} \\ \tau_{xy} \end{bmatrix} = \begin{bmatrix} \bar{Q}_{11} & \bar{Q}_{12} & 0 & 0 & \bar{Q}_{16} \\ \bar{Q}_{12} & \bar{Q}_{22} & 0 & 0 & \bar{Q}_{26} \\ 0 & 0 & \bar{Q}_{44} & \bar{Q}_{45} & 0 \\ 0 & 0 & \bar{Q}_{45} & \bar{Q}_{55} & 0 \\ \bar{Q}_{16} & \bar{Q}_{26} & 0 & 0 & \bar{Q}_{66} \end{bmatrix} \begin{bmatrix} \varepsilon_{xx} \\ \varepsilon_{yy} \\ \varepsilon_{yz} \\ \varepsilon_{xz} \\ \varepsilon_{xy} \end{bmatrix}$$

Figure 5. Deformation of plate in various plate theories.

$$- \begin{bmatrix} 0 & 0 & \bar{e}_{31} \\ 0 & 0 & \bar{e}_{32} \\ \bar{e}_{14} & \bar{e}_{24} & 0 \\ \bar{e}_{15} & \bar{e}_{25} & 0 \\ 0 & 0 & \bar{e}_{36} \end{bmatrix} \begin{bmatrix} E_x \\ E_y \\ E_z \end{bmatrix} \tag{4}$$

$$\begin{bmatrix} D_x \\ D_y \\ D_z \end{bmatrix} = \begin{bmatrix} 0 & 0 & \bar{e}_{14} & \bar{e}_{15} & 0 \\ 0 & 0 & \bar{e}_{24} & \bar{e}_{25} & 0 \\ \bar{e}_{31} & \bar{e}_{32} & 0 & 0 & \bar{e}_{36} \end{bmatrix} \begin{bmatrix} \varepsilon_{xx} \\ \varepsilon_{yy} \\ \varepsilon_{yz} \\ \varepsilon_{xz} \\ \varepsilon_{xy} \end{bmatrix}$$
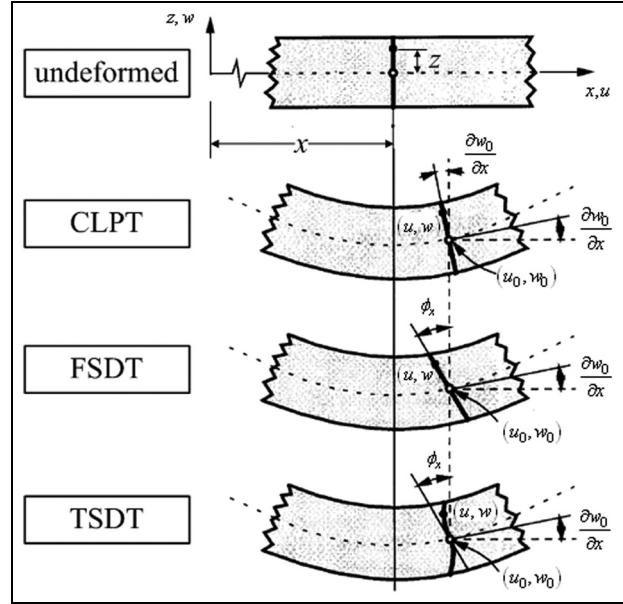
$$+ \begin{bmatrix} \bar{\xi}_{xx}^S & \bar{\xi}_{xy}^S & 0 \\ \bar{\xi}_{xy}^S & \bar{\xi}_{yy}^S & 0 \\ 0 & 0 & \bar{\xi}_{zz}^S \end{bmatrix} \begin{bmatrix} E_x \\ E_y \\ E_z \end{bmatrix} \tag{5}$$

where $[\sigma] = [\sigma_{xx}, \sigma_{yy}, \tau_{yz}, \tau_{xz}, \tau_{xy}]^T$ and $[\varepsilon] = [\varepsilon_{xx}, \varepsilon_{yy}, \gamma_{yz}, \gamma_{xz}, \gamma_{xy}]^T$ are the stress and strain vectors, respectively; $[E] = [E_x, E_y, E_z]^T$ and $[D] = [D_x, D_y, D_z]^T$ are the electric field and electric displacement vector, respectively; $\bar{e}_{ij}$ are the piezoelectric stress coefficients; $\bar{\xi}_{ij}^S$ are the dielectric constants; and $\bar{Q}_{ij}, \bar{e}_{ij}, \bar{\xi}_{ij}^S$ are functions of ply angle θ and are given by Reddy (2004). For the nonpiezoelectric materials, such as facesheets and honeycomb core, the piezoelectric stress coefficients and dielectric constants are set to zeros. The regular hexagonal aluminum honeycomb core possesses orthotropic property, and its equivalent elastic constants are given by Gibson et al. (1982).

The electric field vector $[E]$ is the negative gradient of the electric potential

$$[E] = - \nabla[\varphi] \tag{6}$$

Assuming that the electric field is imposed on the thickness direction and the electric field is described as a linear function, thus

$$[E] = [E_x, E_y, E_z]^T = \left[0, 0, -\frac{\varphi_k}{t_k}\right]^T = -[B_\varphi][\varphi] \quad (7)$$

where t_k is the thickness of the kth layer.

Variational formulation

This formulation will be derived from the Hamilton variational principle in which the strain energy, kinetic energy, and work are considered for the entire structure. The advantage of this method is that it accounts for the physics of the entire structure simultaneously (Chee et al., 1999, 2000). The general form of the Hamilton variational principle is stated as

$$\delta \int_{t_1}^{t_2} (L + W) dt = 0 \quad (8)$$

where $L = K - P$ is the Lagrange function, K is the kinetic energy, P is the potential energy, and W is the external work.

The potential energy can be expressed in terms of virtual strains and electric fields as

$$\delta P = \int_V \left(\delta[\varepsilon]^T[\bar{Q}][\varepsilon] - \delta[\varepsilon]^T[\bar{e}]^T[E] - \delta[E]^T[\bar{e}][\varepsilon] - \delta[E]^T[\bar{\xi}][E] \right) dV \quad (9)$$

The virtual external work of the structure can be given by

$$\delta W = [\delta u, \delta v, \delta w] \begin{bmatrix} F_u^P \\ F_v^P \\ F_w^P \end{bmatrix} + \int_S [\delta u, \delta v, \delta w] \begin{bmatrix} F_u^S \\ F_v^S \\ F_w^S \end{bmatrix} dS$$
$$+ \int_V [\delta u, \delta v, \delta w] \begin{bmatrix} F_u^V \\ F_v^V \\ F_w^V \end{bmatrix} dV - \int_S \delta\varphi Q^S dS \quad (10)$$

where F^V, F^S, and F^P are the volume forces, surface forces, and point forces, respectively, and Q^S is the electrical charges. The dynamic characteristics of the smart reflector will not be considered in the present work, so the kinetic energy will not be elaborated here.

Finite element formulations

The strain components (see equations (2) and (3)) contain first-order derivatives of (u_0, v_0) and (φ_x, φ_y) and second-order derivatives of w_0 with respect to the coordinates x and y. Thus, the displacements (u_0, v_0) and (φ_x, φ_y) should be approximated using the Lagrange interpolation functions, whereas w_0 should be approximated using Hermite interpolation functions. The nonconforming higher-order quadrilateral finite element model is considered here. The element has four nodes, seven degrees of freedom per node, the displacements (u_{0i}, v_{0i}, w_{0i}), the rotations $(\varphi_{xi}, \varphi_{yi})$, and the slopes $((\partial w_0/\partial x)_i, (\partial w_0/\partial y)_i)$.

The displacement field $(u, v, w)^T$ can be expressed using nodal variables $[a^e]$ as follows

$$\begin{bmatrix} u \\ v \\ w \end{bmatrix} =$$
$$[N][a^e] = \left([B_f(\xi, \eta)] + z[B_g(\xi, \eta)] - c_1 z^3 [B_h(\xi, \eta)] \right)[a^e] \quad (11)$$

where $[N]$ is the shape function matrix, $[a^e] = [a_1^T, a_2^T, a_3^T, a_4^T]^T$ are the nodal variables, and $[a_i] = [u_{0i}, v_{0i}, w_{0i}, \varphi_{xi}, \varphi_{yi}, (\partial w/\partial x)_i, (\partial w/\partial y)_i]^T$. The matrices $[B_f(\xi, \eta)]$, $[B_g(\xi, \eta)]$, and $[B_h(\xi, \eta)]$ are defined in Appendix 1.

The strain components $(\varepsilon_{xx}, \varepsilon_{yy}, \gamma_{xy})^T$ and $(\gamma_{yz}, \gamma_{xz})^T$ can be expressed using nodal variables $[a^e]$ as follows

$$[\varepsilon] = \begin{bmatrix} \varepsilon_{xx} \\ \varepsilon_{yy} \\ \gamma_{xy} \\ \gamma_{yz} \\ \gamma_{xz} \end{bmatrix} = [B][a^e]$$
$$= \begin{bmatrix} [B_a(\xi, \eta)] + z[B_b(\xi, \eta)] - c_1 z^3 [B_d(\xi, \eta)] \\ (1 - 3c_1 z^2)[B_c(\xi, \eta)] \end{bmatrix}[a^e] \quad (12)$$

where the matrices $[B_a(\xi, \eta)]$, $[B_b(\xi, \eta)]$, $[B_c(\xi, \eta)]$, and $[B_d(\xi, \eta)]$ are defined in Appendix 1.

The potential energy P and virtual external work W can be expressed using nodal variables $[a^e]$ as follows

$$\delta P = \delta[a^e]^T \int_V [B]^T[\bar{Q}][B] dV[a^e] + \delta[a^e]^T \int_V [B]^T[\bar{e}]^T[B_\varphi] dV[\varphi_e]$$
$$+ \delta[\varphi_e]^T \int_V [B_\varphi]^T[\bar{e}][B] dV[a^e] + \delta[\varphi_e]^T \int_V [B_\varphi]^T[\bar{\xi}_{zz}^S][B_\varphi] dV[\varphi_e] \quad (13)$$

$$\delta W = \delta[a^e]^T[N]^T[F_T^e] - \delta[\varphi_e]^T[Q_T^e] \quad (14)$$

where the superscript e denotes the element number.

The Hamilton variational principle can now be applied using equations (13) and (14) to obtain the final governing equation of the structure system, as follows

$$\int_{t_1}^{t_2} \sum_{e=1}^{n} \left(\begin{array}{c} \delta[a^e]^T[K_{uu}^e][a^e] - \delta[a^e]^T[K_{u\varphi}^e][\varphi_e] - \delta[\varphi_e]^T[K_{\varphi u}^e][a^e] \\ + \delta[\varphi_e]^T[K_{\varphi\varphi}^e][\varphi_e] + \delta[u_e]^T[F_T^e] - \delta[\varphi_e]^T[Q_T^e] \end{array} \right) dt = 0 \quad (15)$$

where n is the total number of elements; see Appendix 2 for more details about mechanical property matrix.

The general governing equation of equilibrium in global coordinate can be obtained using equation (15) and can be written as

$$\begin{bmatrix} [\tilde{K}_{uu}] & [\tilde{K}_{u\varphi}] \\ [\tilde{K}_{\varphi u}] & -[\tilde{K}_{\varphi\varphi}] \end{bmatrix} \begin{bmatrix} [a] \\ [\varphi] \end{bmatrix} = \begin{bmatrix} [\tilde{F}_T] \\ -[\tilde{Q}_T] \end{bmatrix} \qquad (16)$$

where $[\tilde{K}_{uu}]$ is the global stiffness matrix; $[\tilde{K}_{u\varphi}]$ is the global mechanical electrical coupling matrix; $[\tilde{K}_{\varphi\varphi}]$ is the permittivity matrix; $[a]$ is the displacement vector; $[\varphi]$ is the input voltage vector imposed on the actuators; and $[\tilde{F}_T]$ and $[\tilde{Q}_T]$ are the mechanical load and electrical charge vectors, respectively.

Thus, the general formulation for the smart reflector has been reduced to equation (16). This formulation can model arbitrary laminated composite structures with arbitrary boundary conditions. The robustness of the formulation is that each element of each layer can be made of any material, and in this way, the formulation accounts for the mechanical, electrical, and piezoelectric properties.

Static shape control of smart reflector

During reflector operation, the reflector surfaces are deformed by different types of loads (e.g. gravity, temperature, and wind). The deformations induced by temperature and wind loads occur irregularly; yet the gravity deformation is a permanent influence (Paradies and Hertwig, 1999). For this reason, we mainly focus on finding the optimum voltage of the piezoelectric actuators for the gravity deformation correction in this work.

Root mean square error

In engineering application, we particularly concern with the control precision for the static shape control of the structures. Thereby, the main purpose of the shape control is to make the actuated shape as close as the desired shape.

Generally, to measure the closeness between the actuated shape and the desired shape, we define a generalized shape $[\delta] \in R^m$ as

$$[\delta] = [R][a] \qquad (17)$$

where $[R] \in R^{m \times n}$ is a weighting matrix.

The error between the actuated shape $[\delta]$ and the desired shape $[\delta_d] \in R^m$ can be measured by the square error as

$$f = \|[\delta] - [\delta_d]\|_2^2 = ([\delta] - [\delta_d])^T([\delta] - [\delta_d]) \qquad (18)$$

The mirror surface root mean square (RMS) error Ψ can be expressed as

$$\Psi = \sqrt{\frac{f}{m}} = \sqrt{\frac{1}{m}\sum_{i=1}^{m}(\delta_i - \delta_{di})^2} \qquad (19)$$

where δ_i and δ_{di} are the element of vectors $[\delta]$ and $[\delta_d]$, respectively, and m is the total number of nodes which are applied to define the desired shape.

With the introduction of proper boundary conditions (for this study, they are assumed to be simply supported multi-points), the stiffness matrix $[\tilde{K}_{uu}]$ is nonsingular. Therefore, the relationship between the displacement and control voltage can be expressed as

$$[a] = \left([\tilde{K}_{uu}]\right)^{-1}\left([\tilde{F}_T] - [\tilde{K}_{u\varphi}][\varphi]\right) \qquad (20)$$

Substituting equation (20) into equations (17) and (18), we can obtain

$$f([\varphi]) = [\varphi]^T[A][\varphi] + 2[b]^T[\varphi] + e_0 \qquad (21)$$

where

$$[A] = \left([R]\left[\tilde{K}_{uu}\right]^{-1}\left[\tilde{K}_{u\varphi}\right]\right)^T [R]\left[\tilde{K}_{uu}\right]^{-1}\left[\tilde{K}_{u\varphi}\right] \in R^{n \times n}$$

$$[b] = \left([R]\left[\tilde{K}_{uu}\right]^{-1}\left[\tilde{K}_{u\varphi}\right]\right)^T \left([\delta_d] - [R]\left[\tilde{K}_{uu}\right]^{-1}\left[\tilde{F}_T\right]\right) \in R^{n_v}$$

$$e_0 = \left|[\delta_d] - [R]\left[\tilde{K}_{uu}\right]^{-1}\left[\tilde{F}_T\right]\right|^2$$

$$(22)$$

The square error $f([\varphi])$ is a cost function of control voltage for measuring the closeness between the actuated shape and the desired shape.

Optimal control voltage with minimum root square error

The objective of shape control may be stated as seeking for optimal control voltage $[\varphi^*]$ of piezoelectric actuators to minimize the RMS error Ψ, which is equivalent to minimize the cost function $f([\varphi])$ (see equation (21)).

In this case, the optimal control voltages for shape control problem can be obtained via the unconstrained optimization

$$\min f([\varphi]) = [\varphi]^T[A][\varphi] + 2[b]^T[\varphi] + e_0 \qquad (23)$$

In engineering applications, the input voltage of the piezoelectric actuators must lie within a reasonable range in order to avoid the depolarization or electric breakdown. The model for a constrained case is

$$\begin{aligned} \min &: f([\varphi]) = [\varphi]^T[A][\varphi] + 2[b]^T[\varphi] + e_0 \\ s.t. &: g_i([\varphi]) = \varphi_{\max}^2 - \varphi_i^2 \geq 0, \quad i = 1, 2, \ldots, n_v \end{aligned} \qquad (24)$$

where $\varphi_{\max}$ is the maximum voltage allowed and n_v is the total number of actuators.

To find the optimal control voltage $[\varphi^*]$, construct a function using Lagrange multipliers as follows

$$F([\varphi], y, w, \sigma) = f([\varphi]) - \sum_{i=1}^{n_v} w_i \big(g_i([\varphi]) - y_i^2\big)$$
$$+ \frac{\sigma}{2} \sum_{i=1}^{n_v} \big(g_i([\varphi]) - y_i^2\big)^2 \qquad (25)$$

where y_i ($i = 1, 2, \ldots, n_v$) are the relaxation variables, w_i ($i = 1, 2, \ldots, n_v$) are the Lagrange multipliers, and σ is the penalty factor. The constrained optimization problem (24) can be converted to an unconstrained optimization problem (25) by introducing Lagrange multipliers, relaxation variables, and penalty factor. The *BFGS Quasi-Newton* search method was used here for solving equation (25).

Optimal designs of actuator locations using SA algorithm

The distribution of the actuators required for static shape control may be different, and this leads to the problem of optimal selection of actuator locations. For example, if five actuators are adopted in static shape control of smart reflector which has a total of 148 possible locations (see Figure 6), this will produce $C_{148}^5 = 552{,}689{,}424$ different kinds of patterns. For discrete variable structural optimization problems, a variety of methods including SA can be used (Correia et al., 2001). Compared with gradient-based methods, the main advantage of the SA method is the ability to overcome the premature convergence toward a local optimum. The algorithm's major disadvantage is that solving a complex system may be an extremely slow convergence process, using much more processor time than some conventional algorithms. The SA algorithm is adopted here in determining the optimal locations of the selected actuators.

SA algorithm

The basic concept of SA arises from an analogy of metallurgical annealing. Annealing denotes a physical process in which a solid in a heat bath is melted at high temperatures until all molecules of the melted solid can move freely with respect to one another, followed by cooling until thermal mobility is lost.

The implemented SA procedure employs a random search that generates feasible sets of design variables, accepting not only changes in the design variables that decrease the objective function but also changes that increase it. The latter changes are accepted with a certain probability. The basic function of the SA algorithm can be easily described in the following (Moita et al., 2006).
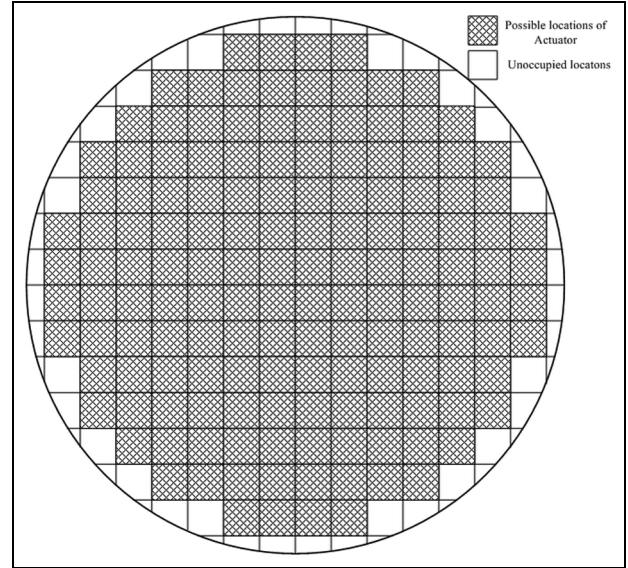

Figure 6. Available locations for actuators.

Generate a random perturbation on the design variables and obtain the change in the objective function $\Delta\Theta$. The Metropolis criterion is used to determine whether the new design variables are accepted and can be expressed as follows

$$P(x_1 \rightarrow x_2) = \begin{cases} 1 & \text{if } \Theta(x_2) < \Theta(x_1) \\ e^{\left(-\frac{\Theta(x_2) - \Theta(x_1)}{T}\right)} & \text{if } \Theta(x_2) \geq \Theta(x_1) \end{cases} \qquad (26)$$

where P is the probability of accepting the new design variables and Θ is an arbitrary cost function.

The parameter T is the temperature, based on the analogy to the physical process of annealing a metal. The initial temperature T_0 and the cooling rate have a great influence on the performance of the algorithm. The initial temperature must be set high enough, so that all proposed states are accepted initially. The cooling schedule can be given by

$$T_{k+1} = \alpha T_k \qquad (27)$$

where T_k and T_{k+1} are the system temperatures at k and $k+1$ successive iterations, respectively, and α is the cooling parameter usually taken in the range of $0.8 - 0.95$. The search is halted when no improvement in the objective function is found combined with the acceptance rate falling below a specified value.

Implementation of SA for selecting the optimal actuator locations

In this section, the application of SA for optimal location of n_v actuators on the M possible locations is discussed. For the optimal locations of the piezoelectric actuators, we consider that each available location for

actuators can only be regular quadrilateral cell corresponding to the finite element mesh discretizaiton. The objective function in this problem is the surface RMS error Ψ, and it is minimized to find the optimal location of the n_v actuators. The design variables $[\Lambda] \in R^{1 \times M}$ are the locations of the actuators and can be defined as follows

$$[\Lambda] = [\lambda_1, \lambda_2, \ldots, \lambda_M]^T \qquad (28)$$

where $\lambda_i \in (0, 1)\, (i = 1 - M)$ is the integer number. There is an actuator in the ith location or not for $\lambda_i = 1$ and $\lambda_i = 0$, respectively.

The solution space of the optimization can be defined as

$$S = \left\{ \Lambda \left| \sum_{i=1}^{M} \lambda_j = n_v, \lambda_i = 0/1 \right. \right\} \qquad (29)$$

Using equations (19), (24), (28), and (29), a general optimization model for optimize n_v actuators location can be stated as

$$find : [\Lambda] = [\lambda_1, \lambda_2, \ldots, \lambda_M]^T$$

$$\min : \Psi([\Lambda]) = \sqrt{\frac{1}{m} \sum_{i=1}^{m} (\delta_i - \delta_{di})^2}$$

$$s.t. : \begin{cases} \sum_{i=1}^{M} \lambda_j = n_v, \lambda_i \in (0, 1) \\ [\tilde{K}_{uu}][a] + [\tilde{K}_{u\varphi}][\varphi] = [\tilde{F}_T] \\ \varphi_{\max}^2 - \varphi_i^2 \geq 0, i = 1, 2, \ldots, n_v \end{cases} \qquad (30)$$

The flowchart for the actuator location optimization process is shown in Figure 7. The optimization model (30) consists of the outer and inner optimization processes. The design variables of the outer process are the locations of actuator, which remain fixed in the inner cycle, while control voltages are the design variables in the inner cycle, described in section "Optimal control voltage with minimum root square error." The flowchart of the inner cycle is shown in Figure 8.

Numerical examples

This section aims to validate the theoretical formulation of the smart reflector and the actuator optimization algorithm by comparing its numerical results with other researchers and to provide some new results.

Model validation

In order to verify the developed model, the following comparisons with other researchers' results are performed.

Case I: piezoelectric laminate beam structure. This preliminary testing with a piezoelectric laminate beam structure is to verify the present modeling method based on the higher-order shear deformation theory. A thick laminate beam consisting of a 15.24-mm-thick aluminum substrate, a 1.524-mm-thick PZT-4 piezoelectric layer, and a 0.254-mm-thick adhesive layer is considered here (Elshafei and Alraiess, 2013). A constant electric potential of 12.5 kV was applied on the upper surface of the piezoelectric layer, and the lower surface was grounded. The predicted values of the transverse displacement along the normalized length of the beam are compared with the results given by Saravanos and Heyliger (1999), Elshafei and Alraiess (2013), and Chee et al. (1999) and are shown in Figure 9. The material properties and the relevant data are same as those in the previous studies.

Figure 9 shows that there is an excellent agreement between the present model and other models, and the minor difference can be attributed to the theoretical formulation.

Case II: smart reflector structure. In order to validate that the presented model is suitable for the smart reflector, a comparison with the results of Paradies et al. (1996) and Wang et al. (2014) is also made. The model considered by Paradies et al. was a flat circle composite plate consisting of eight PXE5 piezoelectric actuator patches which is only fixed at its inner edge, and the numerical simulation is realized using finite element software NASTRAN as shown in Figure 10. The identical model was created using the higher-order shear theory described in the present work and Kirchhoff classical laminated theory described in the authors' previous work (Wang et al., 2014), and different constant electrical fields were applied to every actuator. The RMS error of the plate obtained by these models mentioned above is shown in Figure 11.

Figure 11 shows that the results obtained from the present work share the similar variation pattern with the previous work by the same authors, except that the value in the present one is slightly larger. The slight difference, notable only when the thickness of the structure is large enough, is caused by the fact that the structure modeled by Kirchhoff classical laminated theory is stiffer than that modeled by the higher-order shear theory, which results from the negligence of the shear deformation in the former theory. In addition, Figure 11 also indicates that there is a consistence between the results in authors' work and those in Paradies et al. (1996).

Effect of reflector thickness and facesheet ply thickness on surface RMS error

In this section, a smart reflector (see Figure 1) described in section "Finite element formulation of smart reflector" is considered. There are three constrained nodes,
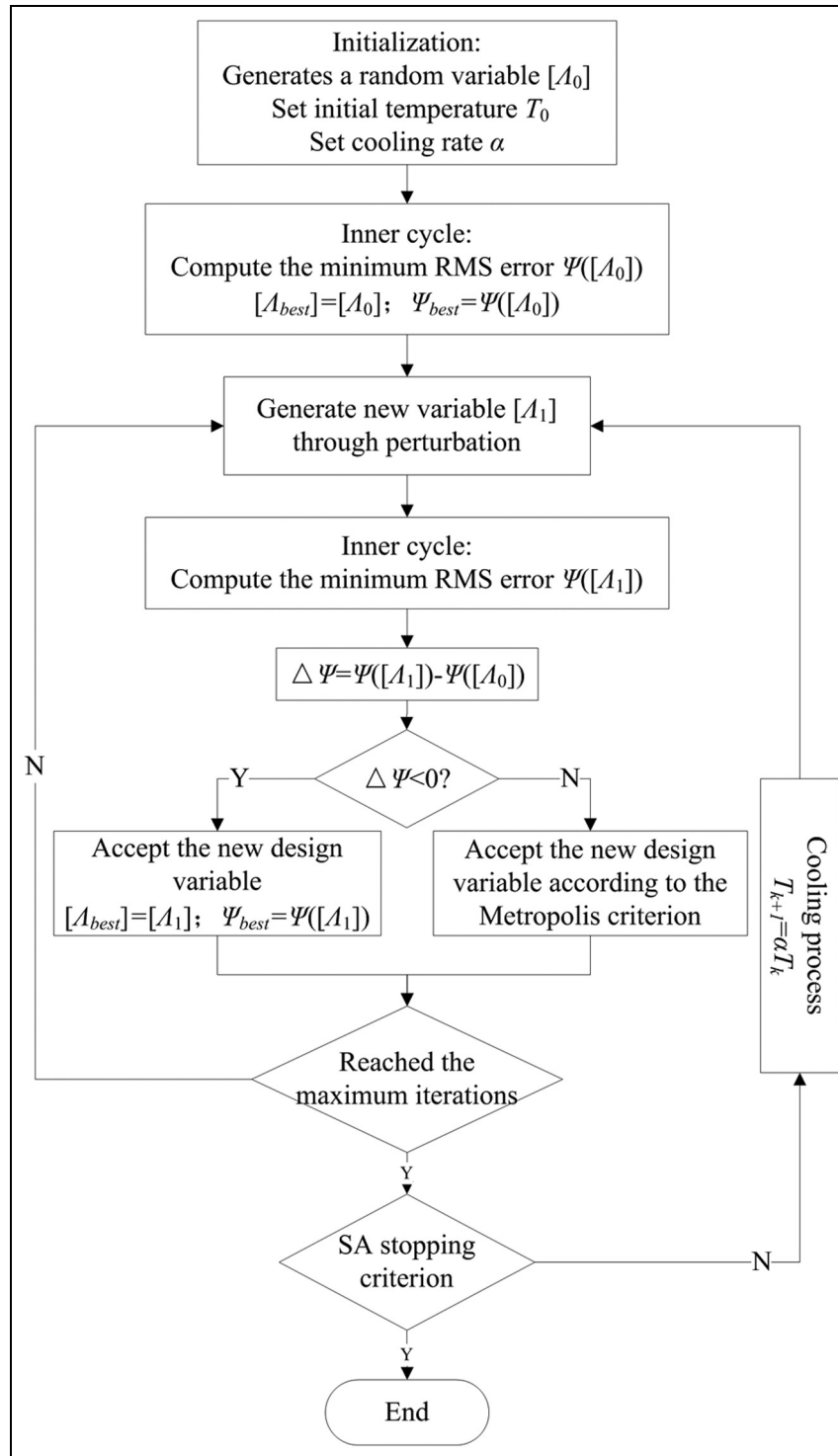
Figure 7. Flowchart for the actuator location optimization.

and the optimum support point location can be determined according to Nelson et al. (1982). The diameter of smart mirror is 300 mm. The material properties and geometry parameters of facesheet, honeycomb core, and actuators are listed in Tables 1 and 2, respectively.

In order to study the effect of reflector thickness and facesheet ply thickness on surface RMS error, the analysis for different thicknesses is presented, and the results are shown in Figure 12. Figure 12 shows that the surface RMS error decreases as the reflector thickness increases, and the surface RMS error increases as the facesheet ply thickness increases accordingly. Thus, the thickness of reflector and facesheet ply can be determined initially as 25 and 0.06 mm, respectively.
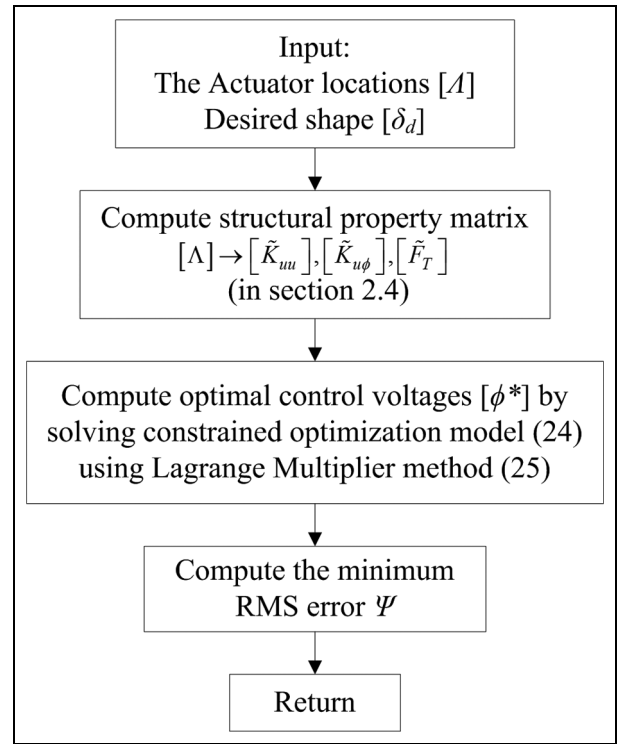
Figure 8. Flowchart of the inner cycle.

Figure 10. Mesh model of flat plate.

Figure 9. Deflection of the beam along normalized axial location.
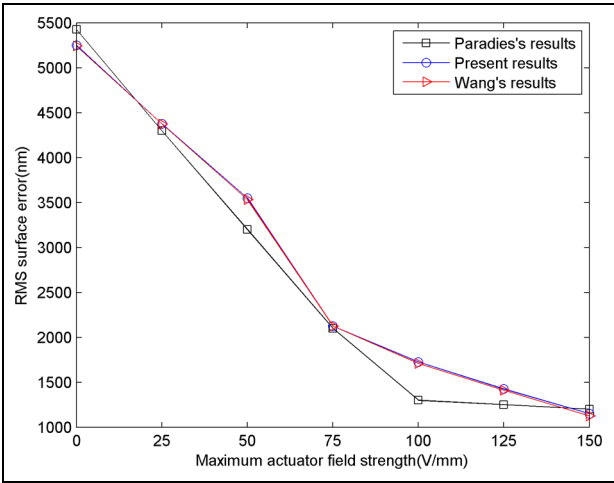
Figure 11. Simulation results comparison.

Table 2. Geometry parameters.

	Facesheet ply	Honeycomb wall	PZT-5A
Number of plies	16	–	–
Stacking sequence	$[\pm 27/\pm 74]_s/$ $[\mp 27/\mp 74]_s$	–	–
Length (mm)	20	9.53	20
Width (mm)	20	–	20
Thickness (mm)	–	0.07	0.4

Optimal design of actuator locations

In this section, the application of the SA for optimal design of actuator locations in static shape control of smart reflector (see Figure 1) is studied. The material
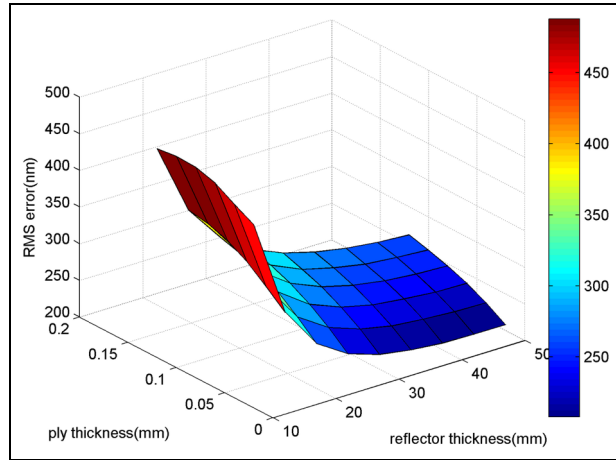
Table 1. Material properties.

	Facesheet ply	Honeycomb wall	PZT-5A
E_1 (GPa)	209.0	70	61.5
E_2 (GPa)	9.02	70	61.5
v_{12}	0.3	0.3	0.441
G_{12} (GPa)	4.7	26.9	22.6
G_{13} (GPa)	–	–	21.1
G_{23} (GPa)	–	–	21.1
d_{31} (mm/V)	–	–	-171×10^{-9}
d_{32} (mm/V)	–	–	-171×10^{-9}
ρ (kg/m^3)	1850	2700	7750
Vmax (V)			± 150

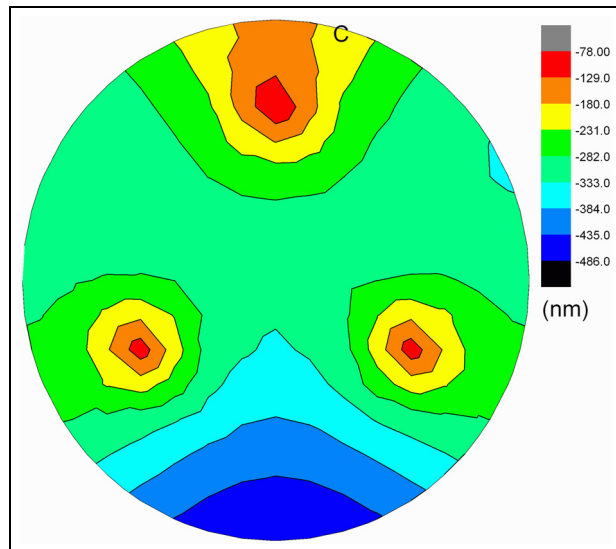**Figure 12.** RMS versus reflector thickness and ply thickness.

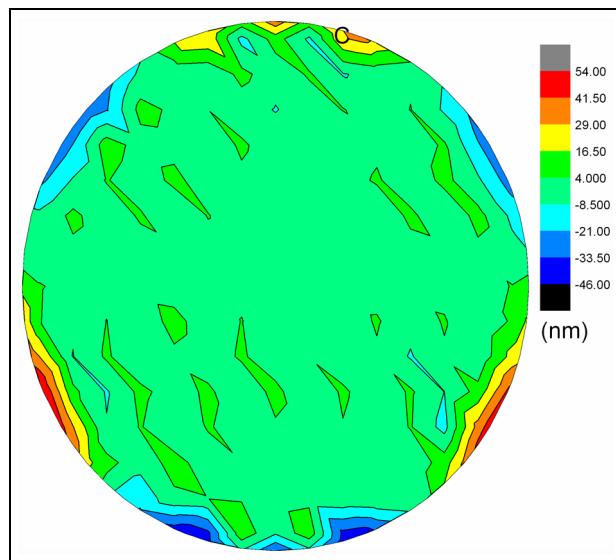**Figure 13.** Uncontrolled deformation of smart reflector.

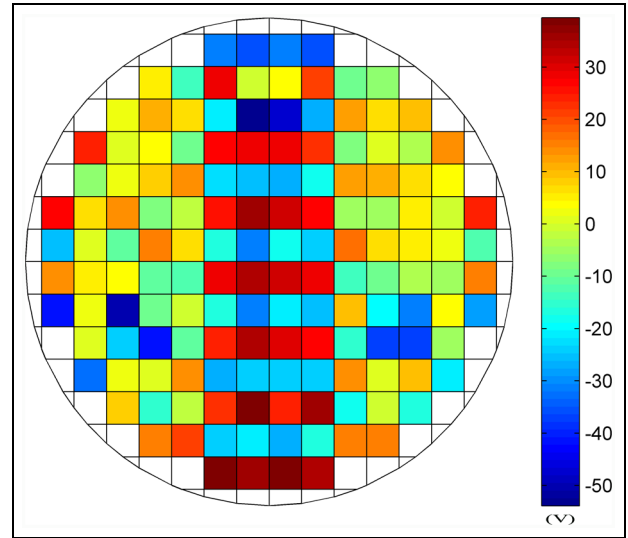**Figure 14.** Controlled deformation of smart reflector.

Figure 15. Voltage of actuators.

properties and relevant parameters are given in section "Effect of reflector thickness and facesheet ply thickness on surface RMS error." The following simulations are divided into three categories:

Case I. All possible locations are covered by actuators, to verify the performance of static shape control by actuation;
Case II. Optimization of n_v (n_v is arbitrary number) actuator location. To verify the performance of SA for optimize actuator locations;
Case III. Investigation of the effect of actuator numbers on RMS error.

Due to the gravity, the smart reflector will have relative large deformation without any shape control. The RMS error reaches 304.5 nm, and the gravity deformation contour without control is shown in Figure 13.

All possible locations are covered by actuators. Here, we discuss one extreme condition that all possible locations are covered by actuators, that is, there are altogether 148 (see Figure 6) actuators placed in the smart reflector. To perform static shape control, the weighting factors in the weight matrix $[R]$ corresponding the transverse displacements at all nodes, which means that only the transverse displacement is taken into account in the shape control. The objective of the static shape control is to keep all the nodes of the smart reflector in the horizontal plane since a single-layer theory is used. Using Lagrange multiplier method to solve the constrained optimization problem described in equation (24), the optimal control voltage of the actuators can be determined. The actuated shape by imposing the control voltage on the actuators is shown in Figure 14. It can be seen that the controlled shape of smart
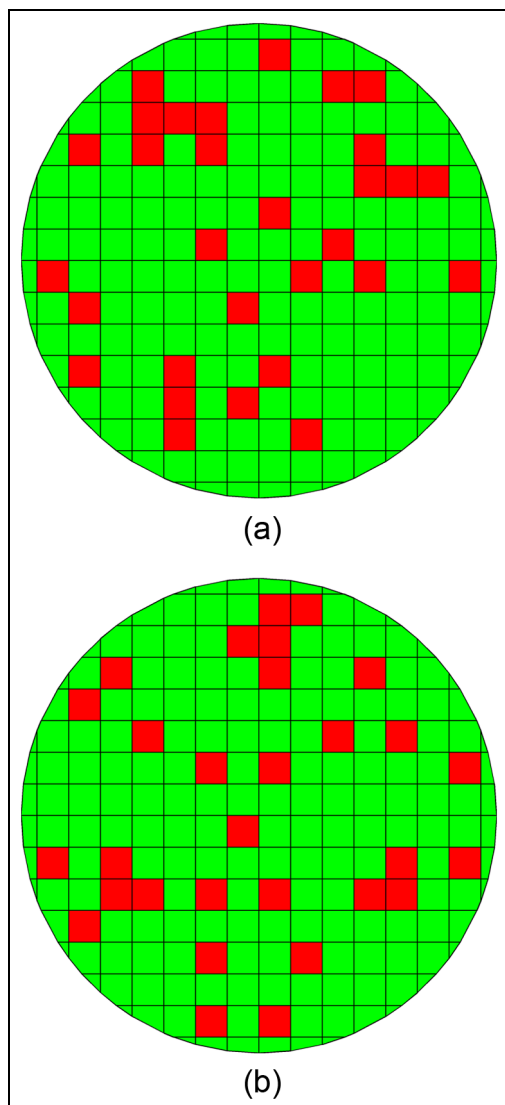
Figure 16. (a) Initial and (b) optimal locations for n_v actuators.

reflector is very close to the desired shape, and the RMS error between the desired shape and controlled shape is 9 nm. The control voltage of actuators is shown in Figure 15.

Optimization of n_v (n_v is arbitrary number) actuator location. In order to verify the performance of SA for optimizing the locations of actuator, the following simulation test was presented. Consider the smart reflector placing n_v (here n_v = 30) actuators on the bottom facesheet. To optimize the location of n_v actuators using SA algorithm discussed in section "Optimal designs of actuator locations using SA algorithm," the layouts of initial and final optimal locations of n_v actuators are shown in Figure 16. The variation of objective function (RMS) during the optimization iterations is shown in Figure 17. Figure 18 shows the new design variables accepted or dropped in each

iteration (0: dropped, 1: accepted). The cooling cycles of SA during optimization are shown in Figure 19.

The RMS error between the desired shape and controlled shape reaches 22 nm when the n_v (here n_v = 30) actuators are placed on the optimal locations. The controlled shape of smart reflector and control voltage of actuators are shown in Figures 20 and 21, respectively.

Compared to the case I (given in section "All possible locations are covered by actuators"), 118 actuators have been removed, while the RMS error has increased only about 5%, which would greatly reduce the cost and do not affect the performance much.

Figure 17 shows that in the whole optimization process, the RMS error is reduced by about 80%, which indicates that the SA algorithm is very efficient for optimizing the location of actuators. As shown in Figures 17 to 19, there are two courses in the whole optimization process. The first one is in between 1st and 20th cooling cycles in Figure 19 (between 0 and 600 iterations in Figures 17 and 18), where the design transitions were carried out within an extensive infeasible design space, also including nonimproving regions under the influence of high temperatures. This value emphasizes the success of the algorithm in effectively searching the design space at the start, indicating to which extent the infeasible regions are considered in this course. Another one is the remaining cooling cycles, where the temperature has decreased, which showed less tolerance to transitions to infeasible design regions.

As shown in Figures 15 and 21, the constraints of control voltages seem not to act on the results, which is because that the deformation of the model mentioned in this work is too small. If the deformation is large enough, the effect of the constraints will be more apparent (Wang et al., 2014).

Investigation of the effect of actuator numbers. In order to investigate the effect of actuator numbers on the RMS error, the following simulation is presented. Consider the smart reflector discussed in section "Optimization of n_v (n_v is arbitrary number) actuators location," placing n_v actuators, where n_v varies from 5 to 120, and using the SA to optimize the location of n_v actuators. The variation of RMS error along actuator numbers is shown in Figure 22.

Figure 22 shows that as the actuator numbers increase, the RMS error decreases accordingly. There are two stages in the whole process. The first stage is in between 5 and 30 actuators, where the RMS error decreases quickly as the actuator numbers increase, which indicate that there is a remarkable effect of actuator numbers on RMS error. Another one is the subsequent actuator numbers, where the RMS error decreases slowly, which indicate that the effect is unremarkable.
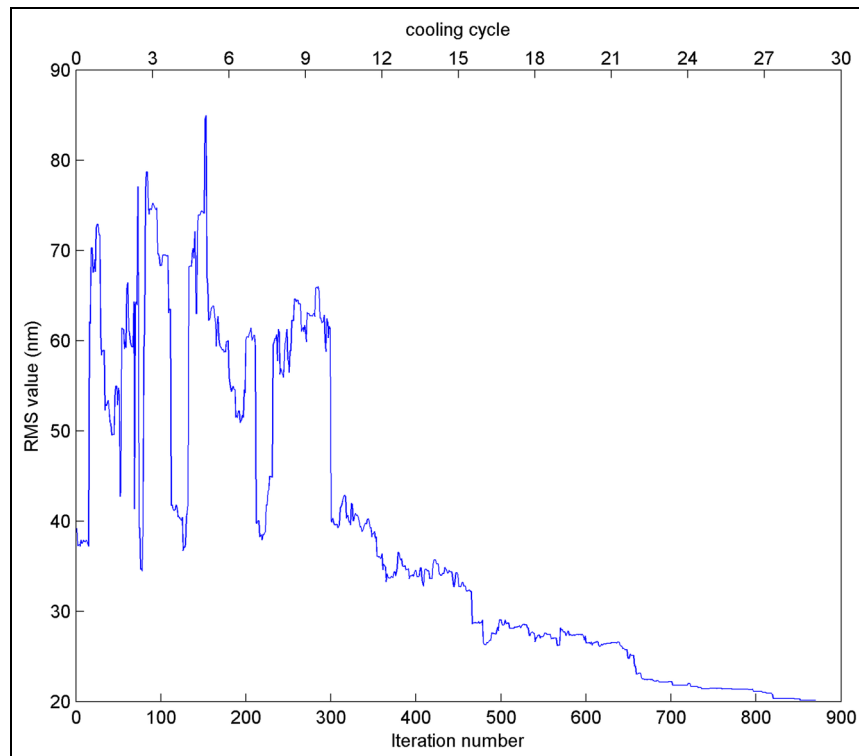
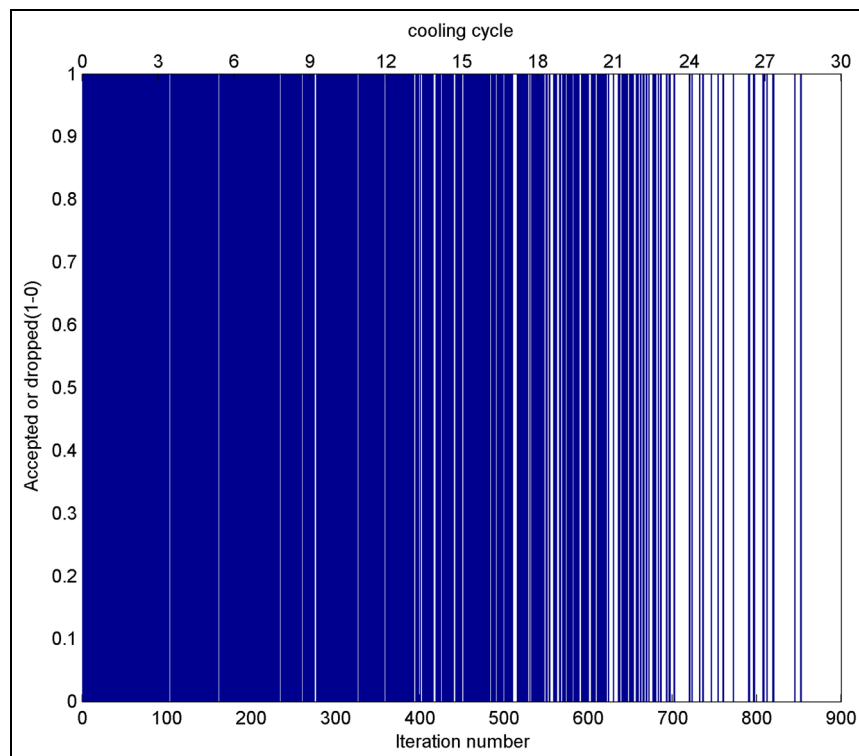**Figure 17.** Variation of objective function during optimization.

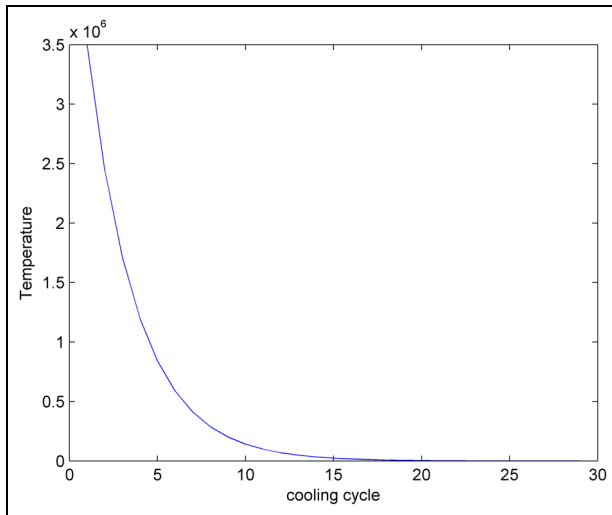**Figure 18.** Accept or drop the new design variables.
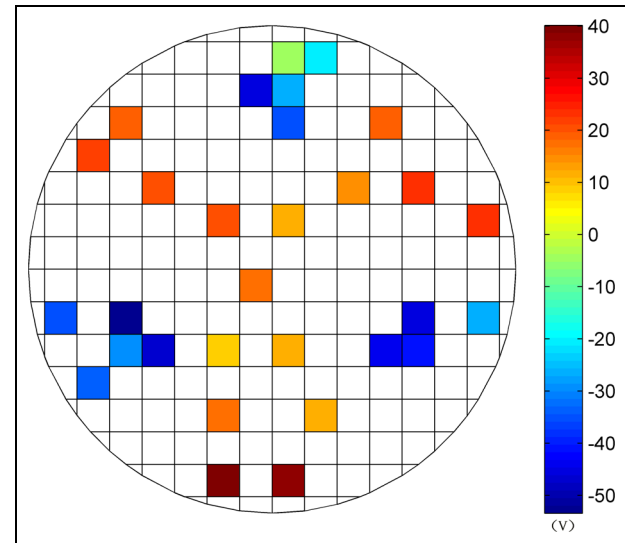
Figure 19. Cooling cycles of SA.
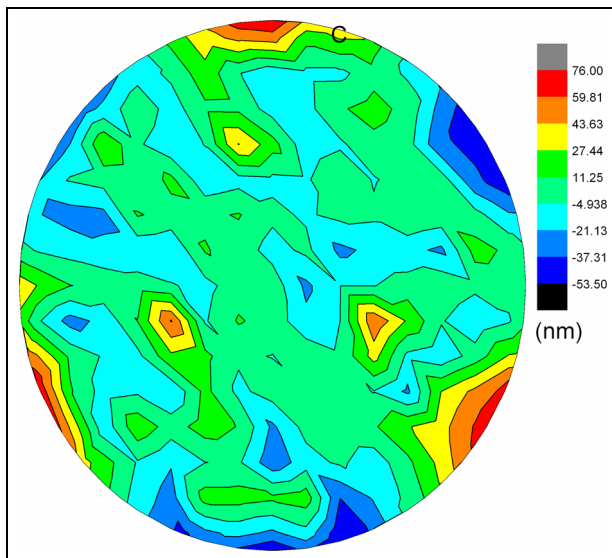

Figure 21. Control voltage of n_v actuators.

Figure 20. Controlled shape of smart reflector.

Figure 22. Relations between actuator numbers and RMS error.

Conclusions

Static shape control and optimal design of smart reflector with distributed piezoelectric actuators has been investigated based on the higher-order shear deformation theory. The finite element model considering electromechanical coupling effect is derived using the Hamilton variational principle. The optimization model for determining the optimal control voltages is presented, and the Lagrange multipliers are employed to deal with the voltage limitation. The optimal design of actuator locations using SA algorithm is also investigated.

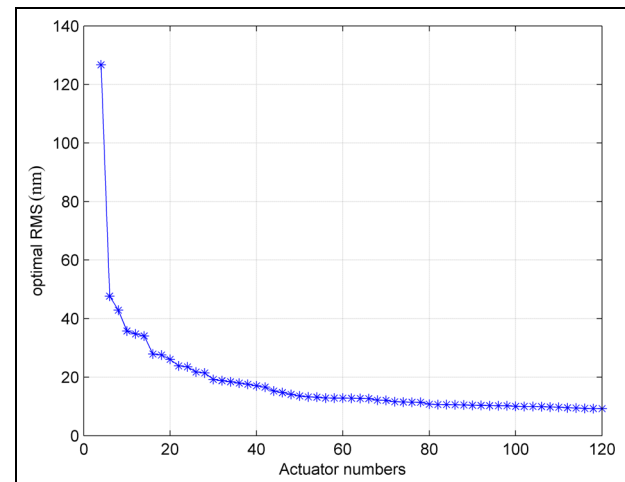Numerical examples of smart beam are given based on the presented finite model, and the obtained results correlated well with other published results. For the smart reflector, the effect of reflector thickness and facesheet ply thickness on surface root square error is investigated, and the results show that the surface root square error decreases as the reflector thickness increases, and reversely, the surface root square error increases as the facesheet ply thickness increases. The application of the SA for optimal design of actuator locations is studied in three categories. The results show that the finite element model and the Lagrange multiplier method are very effective in static shape control of smart reflector, and the actuator locations and numbers have a great effect on the RMS error.

Declaration of conflicting interests

The author(s) declared no potential conflicts of interest with respect to the research, authorship, and/or publication of this article.

References

Balamurugan V and Narayanan S (2007) A piezoelectric higher-order plate element for the analysis of multi-layer smart composite laminates. *Smart Materials and Structures* 16(6): 2026–2039.

Chee C, Tong L and Steven G (1999) A mixed model for composite beams with piezoelectric actuators and sensors. *Smart Materials and Structures* 8(3): 417–432.

Chee C, Tong L and Steven G (2000) A mixed model for adaptive composite plates with piezoelectric for anisotropic actuation. *Computers & Structures* 77(3): 253–268.

Chee C, Tong L and Steven G (2002) Static shape control of composite plates using a slope-displacement based algorithm. *AIAA Journal* 40(8): 1611–1618.

Chen PC and Romeo RC (2004) Advances in composite mirror and telescope technology. *Proceedings of SPIE* 5382(1): 397–403.

Chen PC, Bowers CW, Content DA, et al. (2000) Advances in very lightweight composite mirror technology. *Optical Engineering* 39(9): 2320–2329.

Correia VMF, Mota SCM and Mota SCA (2001) Refined models for the optimal design of adaptive structures using simulated annealing. *Composite Structures* 54(2–3): 161–167.

Elshafei MA and Alraiess F (2013) Modeling and analysis of smart piezoelectric beams using simple higher order shear deformation theory. *Smart Materials and Structures* 22(3): 035006.

Frecker MI (2003) Recent advances in optimization of smart structures and actuators. *Journal of Intelligent Material Systems and Structures* 14(4–5): 207–216.

Gibson LJ, Ashby MF, Schajer GS, et al. (1982) The mechanics of two-dimensional cellular materials. *Proceedings of the Royal Society of London A: Mathematical and Physical Sciences* 382(1782): 25–42.

Gupta V, Sharma M and Thakur N (2010) Optimization criteria for optimal placement of piezoelectric sensors and actuators on a smart structure: a technical review. *Journal of Intelligent Material Systems and Structures* 21(12): 1227–1243.

Hwan-Sik Y (2013) Optimal shape control of adaptive structures for performance maximization. *Structural and Multidisciplinary Optimization* 48(3): 571–580.

Hwan-Sik Y and Washington G (2005) Generation of multiple beam patterns using a mechanically reconfigurable smart reflector antenna system. *AIAA Journal of Aerospace Computing, Information, and Communication* 2(5): 252–266.

Hwan-Sik Y and Washington G (2010) An optimal method of shape control for deformable structures with an application to a mechanically reconfigurable reflector antenna. *Smart Materials and Structures* 19(10): 105004.

Kapuria S, Kumari P and Nath JK (2010) Efficient modeling of smart piezoelectric composite laminates: a review. *Acta Mechanica* 214(1–2): 31–48.

Khandan R, Noroozi S, Sewell P, et al. (2012) The development of laminated composite plate theories: a review. *Journal of Materials Science* 47(16): 5901–5910.

Lage RG, Soares CMM, Soares CAM, et al. (2004) Modelling of piezolaminated plates using layerwise mixed finite elements. *Computers & Structures* 82(23–26): 1849–1863.

Liu CH (1993) *Structural analysis and design of adaptive lightweight mirrors.* MS Thesis, Massachusetts Institute of Technology, Cambridge, MA.

Mehta PK (1990) Moment actuator influence function for flat circular deformable mirrors. *Advances in Optical Structure Systems* 29(10): 1213–1222.

Moita JMS, Correia VMF, Martins PG, et al. (2006) Optimal design in vibration control of adaptive structures using a simulated annealing algorithm. *Composite Structures* 75(1): 79–87.

Moita JS, Martins PG, Mota Soares CM, et al. (2008) Optimal dynamic control of laminated adaptive structures using a higher order model and a genetic algorithm. *Computers & Structures* 86(3–5): 198–206.

Nelson JE, Lubliner J and Mast TS (1982) Telescope mirror supports: plate deflections on point supports. *Advanced Technology Optical Telescopes* 332(10): 212–228.

Paradies R and Hertwig M (1999) Shape control of adaptive composite reflectors. *Composites Part B: Engineering* 30(1): 65–78.

Paradies R, Hertwig M and Elspass WJ (1996) Shape control of an adaptive mirror at different angles of inclination. *Journal of Intelligent Material Systems and Structures* 7(2): 203–210.

Reddy JN (1999) On laminated composite plates with integrated sensors and actuators. *Engineering Structures* 21(7): 568–593.

Reddy JN (2004) *Mechanics of Laminated Composite Plates and Shells: Theory and Analysis.* New York: CRC Press.

Saravanos DA and Heyliger PR (1999) Mechanics and computational models for laminated piezoelectric beams, plates, and shells. *Applied Mechanics Reviews* 52(10): 305–320.

Sun D and Tong L (2005) Design optimization of piezoelectric actuator patterns for static shape control of smart plates. *Smart Materials and Structures* 14(6): 1353–1362.

Wang Z and Li T (2014) Optimal piezoelectric sensor/actuator placement of cable net structures using H_2-norm measures. *Journal of Vibration and Control* 20(8): 1257–1268.

Wang Z, Cao Y, Zhou C, et al. (2014) Static shape control of flexible piezoelectric smart reflectors. *Optics and Precision Engineering* 22(10): 2715–2724.

Appendix I

The shape functions

$$[N] = [J(z)][Nu(\xi, \eta)] \tag{31}$$

$$J(z) = \begin{bmatrix} 1 & 0 & -c_1 z^3 \frac{\partial}{\partial x} & z - c_1 z^3 & 0 \\ 0 & 1 & -c_1 z^3 \frac{\partial}{\partial y} & 0 & z - c_1 z^3 \\ 0 & 0 & 1 & 0 & 0 \end{bmatrix} \tag{32}$$

$$[Nu_i] = \begin{bmatrix} N_i & 0 & 0 & 0 & 0 & 0 & 0 \\ 0 & N_i & 0 & 0 & 0 & 0 & 0 \\ 0 & 0 & H_i^{(0)} & 0 & 0 & H_i^{(1x)} & H_i^{(1y)} \\ 0 & 0 & 0 & N_i & 0 & 0 & 0 \\ 0 & 0 & 0 & 0 & N_i & 0 & 0 \end{bmatrix} \tag{33}$$

$$N_i = \frac{1}{4}(1 + \xi_i\xi)(1 + \eta_i\eta) \tag{34}$$

$$H_i^{(0)} = \frac{1}{8}(1 + \xi_i\xi)(1 + \eta_i\eta)(2 + \xi_i\xi + \eta_i\eta - \xi^2 - \eta^2) \tag{35}$$

$$H_i^{(1x)} = \frac{1}{8}\xi_i(\xi_i\xi - 1)(1 + \eta_i\eta)(1 + \xi_i\xi)^2 \tag{36}$$

$$H_i^{(1y)} = \frac{1}{8}\eta_i(\eta_i\eta - 1)(1 + \xi_i\xi)(1 + \eta_i\eta)^2 \tag{37}$$

where ξ and η are general coordinates; N_i and $H_i^{(*)}$ are Lagrange interpolation functions and Hermite interpolation functions, respectively; and $i = 1, 2, 3, 4$.

The B-matrices

$$[B_\gamma(\xi, \eta)] = [B_{\gamma 1}, B_{\gamma 2}, B_{\gamma 3}, B_{\gamma 4}] \tag{38}$$

where $\gamma = a, b, c, d, f, g, h$

$$[B_{ai}] = \begin{bmatrix} \frac{\partial N_i}{\partial x} & 0 & 0 & 0 & 0 & 0 & 0 \\ 0 & \frac{\partial N_i}{\partial y} & 0 & 0 & 0 & 0 & 0 \\ \frac{\partial N_i}{\partial y} & \frac{\partial N_i}{\partial x} & 0 & 0 & 0 & 0 & 0 \end{bmatrix} \tag{39}$$

$$[B_{bi}] = \begin{bmatrix} 0 & 0 & 0 & \frac{\partial N_i}{\partial x} & 0 & 0 & 0 \\ 0 & 0 & 0 & 0 & \frac{\partial N_i}{\partial y} & 0 & 0 \\ 0 & 0 & 0 & \frac{\partial N_i}{\partial y} & \frac{\partial N_i}{\partial x} & 0 & 0 \end{bmatrix} \tag{40}$$

$$[B_{ci}] = \begin{bmatrix} 0 & 0 & \frac{\partial H_i^{(0)}}{\partial y} & 0 & N_i & \frac{\partial H_i^{(1x)}}{\partial y} & \frac{\partial H_i^{(1y)}}{\partial y} \\ 0 & 0 & \frac{\partial H_i^{(0)}}{\partial x} & N_i & 0 & \frac{\partial H_i^{(1x)}}{\partial x} & \frac{\partial H_i^{(1y)}}{\partial x} \end{bmatrix} \tag{41}$$

$$[B_{di}] = \begin{bmatrix} 0 & 0 & \frac{\partial^2 H_i^{(0)}}{\partial x^2} & \frac{\partial N_i}{\partial x} & 0 & \frac{\partial^2 H_i^{(1x)}}{\partial x^2} & \frac{\partial^2 H_i^{(1y)}}{\partial x^2} \\ 0 & 0 & \frac{\partial^2 H_i^{(0)}}{\partial y^2} & 0 & \frac{\partial N_i}{\partial y} & \frac{\partial^2 H_i^{(1x)}}{\partial y^2} & \frac{\partial^2 H_i^{(1y)}}{\partial y^2} \\ 0 & 0 & 2\frac{\partial^2 H_i^{(0)}}{\partial x \partial y} & \frac{\partial N_i}{\partial y} & \frac{\partial N_i}{\partial x} & 2\frac{\partial^2 H_i^{(1x)}}{\partial x \partial y} & 2\frac{\partial^2 H_i^{(1y)}}{\partial x \partial y} \end{bmatrix} \tag{42}$$

$$[B_{fi}] = \begin{bmatrix} N_i & 0 & 0 & 0 & 0 & 0 & 0 \\ 0 & N_i & 0 & 0 & 0 & 0 & 0 \\ 0 & 0 & H_i^{(0)} & 0 & 0 & H_i^{(1x)} & H_i^{(1y)} \end{bmatrix} \tag{43}$$

$$[B_{gi}] = \begin{bmatrix} 0 & 0 & 0 & N_i & 0 & 0 & 0 \\ 0 & 0 & 0 & 0 & N_i & 0 & 0 \\ 0 & 0 & 0 & 0 & 0 & 0 & 0 \end{bmatrix} \tag{44}$$

$$[B_{hi}] = \begin{bmatrix} 0 & 0 & \frac{\partial H_i^{(0)}}{\partial x} & N_i & 0 & \frac{\partial H_i^{(1x)}}{\partial x} & \frac{\partial H_i^{(1y)}}{\partial x} \\ 0 & 0 & \frac{\partial H_i^{(0)}}{\partial y} & 0 & N_i & \frac{\partial H_i^{(1x)}}{\partial y} & \frac{\partial H_i^{(1y)}}{\partial y} \\ 0 & 0 & 0 & 0 & 0 & 0 & 0 \end{bmatrix} \tag{45}$$

Appendix 2

The mechanical property matrices

$$K_{uu}^e = \sum_{k=1}^{nlayer} \int_{\xi=-1}^{+1} \int_{\eta=-1}^{+1} \int_{z=z_k}^{z=z_{k+1}} (B\bar{Q}B)\frac{\partial(x,y)}{\partial(\xi,\eta)} dz d\eta d\xi \tag{46}$$

$$K_{u\varphi}^e = \sum_{k=1}^{nlayer} \int_{\xi=-1}^{+1} \int_{\eta=-1}^{+1} \int_{z=z_k}^{z=z_{k+1}} (B\bar{e}B_\varphi)\frac{\partial(x,y)}{\partial(\xi,\eta)} dz d\eta d\xi \tag{47}$$

$$K_{\varphi\varphi}^e = \sum_{k=1}^{nlayer} \int_{\xi=-1}^{+1} \int_{\eta=-1}^{+1} \int_{z=z_k}^{z=z_{k+1}} (B_\varphi\bar{\xi}_{zz}^S B_\varphi)\frac{\partial(x,y)}{\partial(\xi,\eta)} dz d\eta d\xi \tag{48}$$